ARTICLE

Multispectral Localized Surface Plasmon Resonance (msLSPR) Reveals and Overcomes Spectral and Sensing Heterogeneities of Single Gold Nanoparticles

Stephen Palani, John P. Kenison, Sinan Sabuncu, Tao Huang, Fehmi Civitci, Sadik Esener, and Xiaolin Nan*

Read Online

ACCESS | Metrics & More | Article Recommendations | Supporting Information

ABSTRACT: Metal nanoparticles can be sensitive molecular sensors due to enhanced absorption and scattering of light near a localized surface plasmon resonance (LSPR). Variations in both intrinsic properties such as the geometry and extrinsic properties such as the environment can cause heterogeneity in nanoparticle LSPR and impact the overall sensing responses. To date, however, few studies have examined LSPR and sensing heterogeneities, due to technical challenges in obtaining the full LSPR spectra of individual nanoparticles in dynamic assays. Here, we report multispectral LSPR (msLSPR), a wide-field imaging technique for real-time spectral monitoring of light scattering from individual nanoparticles across the whole field of view (FOV) at ∼0.5 nm spectral and ∼100 ms temporal resolutions. Using msLSPR, we studied the spectral and sensing properties of gold nanoparticles commonly used in LSPR

assays, including spheres, rods, and bipyramids. Complemented with electron microscopy imaging, msLSPR analysis revealed that all classes of gold nanoparticles exhibited variations in LSPR peak wavelengths that largely paralleled variations in morphology. Compared with the rods and spheres, gold nanobipyramids exhibited both more uniform and stronger sensing responses as long as the bipyramids are structurally intact. Simulations incorporating the experimental LSPR properties demonstrate the negative impact of spectral heterogeneity on the overall performance of conventional, intensity-based LSPR assays and the ability of msLSPR in overcoming both particle heterogeneity and measurement noise. These results highlight the importance of spectral heterogeneity in LSPR-based sensors and the potential advantage of performing LSPR assays in the spectral domain.

KEYWORDS: nanoparticles, localized surface plasmon resonance, single particle, dark-field microscopy, multispectral imaging
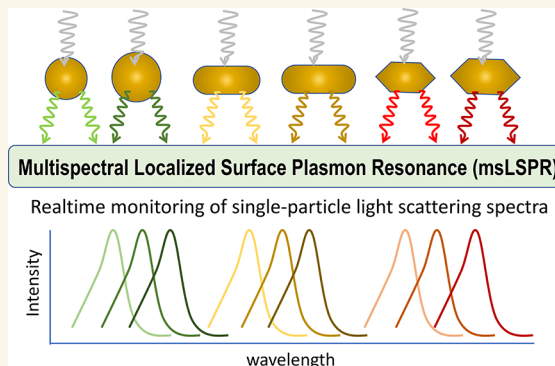
INTRODUCTION

Plasmonic metal nanoparticles possess optical properties that allow them to be versatile materials for label-free biosensors.[1] Unlike the surface-propagating plasmons observed on metal films, nanoparticles with features on the 10−100 nm size scale exhibit a localized surface plasmon resonance (LSPR) that arises from the collective oscillation of conduction electrons confined on the particle surface upon incident electromagnetic radiation. For both a metal film and nanoparticles, the SPR is sensitive to the dielectric constant (or the refractive index) of its immediate environment, which is the basis for label-free molecular sensing.[2,3] Compared with thin-film- or nano-particle-solution-based SPR assays, single-particle LSPR assays

(where the nanoparticles are installed on a substrate and detected individually) offers advantages including higher sensitivity and, potentially, multiplexity.[4,5] For example, single-particle LSPR has been shown to detect single molecules.[6−8] This is because LSPR sensors have smaller and confined sensing volumes, requiring a smaller percentage of
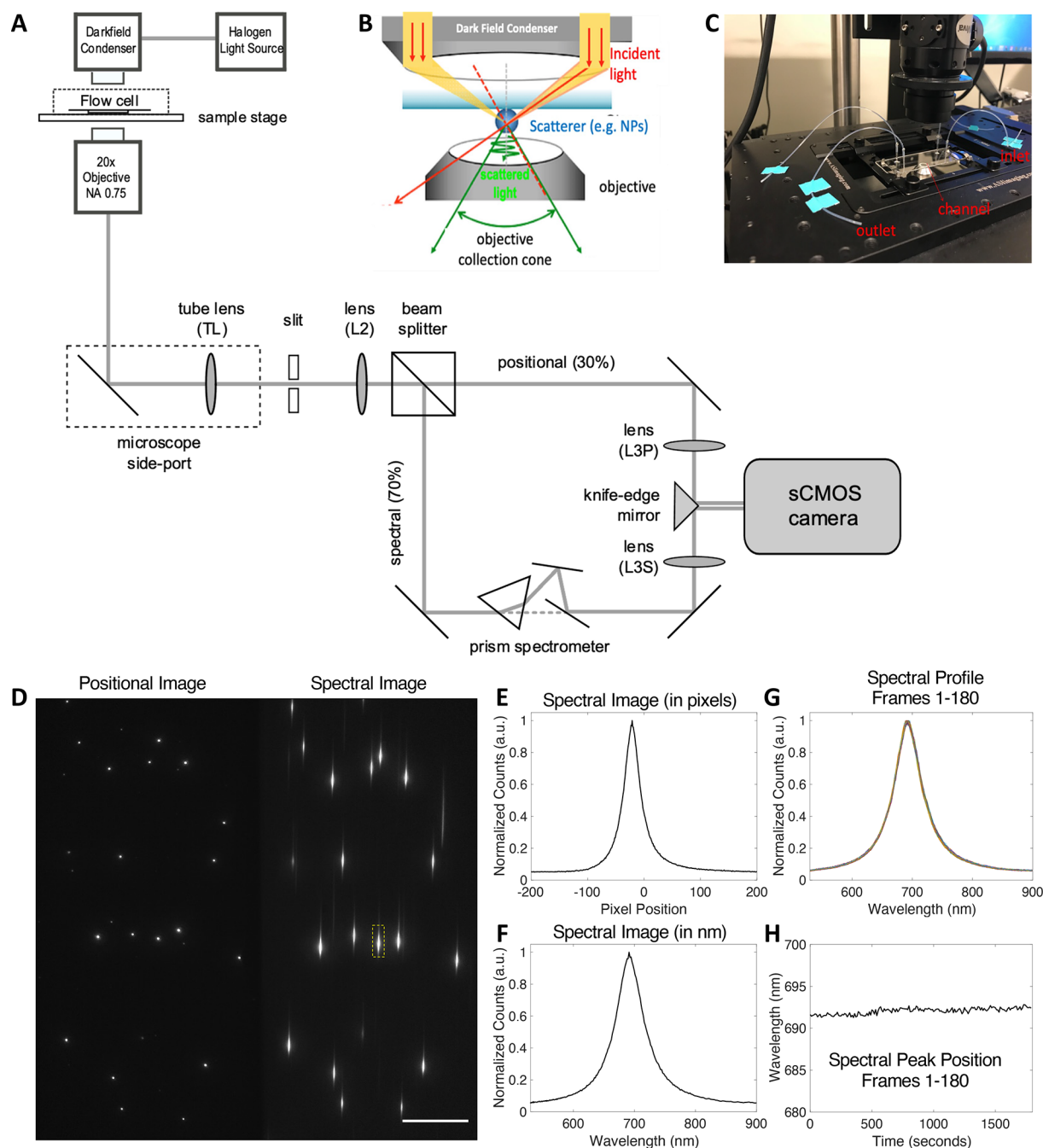
Figure 1. The multispectral localized surface plasmon resonance (msLSPR) imaging setup. (A) Optical scheme of the msLSPR imaging system. **(B)** High signal-to-noise illumination is achieved through a dark-field condenser (NA = 1.4), and wide-field scattering signal collection is achieved through a 20× objective (NA = 0.75). **(C)** Flow cell construction consisting of a top glass slide that contacts the dark-field condenser and bottom glass coverslip sandwich assembly separated by adhesive transfer tape. Teflon tubing and pipette tips provide inlet and outlet functionality. **(D)** Sample field of view from an msLSPR imaging system consisting of positional information (left half) and spectral information for each particle (right half) (scale bar: 30 um). **(E)** LSPR scattering spectrum of a representative particle (boxed in **(D)**) in pixel intensity units. **(F)** LSPR scattering spectrum of the same particle after conversion to wavelength units. **(G)** Monitoring the spectral profile of the particle for all frames to test temporal stability of LSPR spectra. **(H)** Plotting the LSPR peak position after polynomial fitting. For **(G)** and **(H)**, data were acquired for 30 min at 200 ms exposure and a 10 s interval between frames.

surface-bound analytes to generate a signal. Additionally, since the LSPR spectrum is dependent on the size, shape, and composition of the nanoparticle,[9] multiple types of nanoparticles could be used in a single assay to probe many targets at once. These advantages make single-particle LSPR an attractive format in SPR-based molecular sensing.

A major limiting factor in pushing the utility of single-particle LSPR, however, is the heterogeneity in LSPR spectral and sensing properties among the nanoparticles. This heterogeneity can first arise from variations in nanoparticle properties such as size and geometry. Over the past two decades, wet-chemical synthesis of colloidal gold nanoparticles has been carefully refined to produce samples with relatively

good uniformity in shape and size.[10−12] Gold nanospheres, nanorods, and nanobipyramids are commonly used variants because of their structural stability, strong near-field enhancements, and highly controllable geometric parameters based on varying synthesis conditions.[13] Nanorods, and to a greater extent nanobipyramids, have sharp edges and tips for higher field enhancement.[14−20] Despite improvements in chemical synthesis protocols, however, at least some nanoparticle geometries will still exhibit spectral heterogeneity due to geometric variations. Additional variations may be introduced during the fabrication of the single-particle LSPR device such as uneven surfaces and particle aggregation. Multiparticle aggregates exhibit significantly red-shifted resonances due to plasmon hybridization compared with single particles.[21] Furthermore, environmental parameters such as photothermal effects, pH, ionic strength, and oxidation of surface atoms can influence the LSPR properties of the nanoparticles.[22,23] These variations will directly impact the detected LSPR response in terms of signal uniformity and ultimately the detection limit. As such, the ability to characterize the LSPR spectral profile and sensing response of individual nanoparticles will be a key step to harnessing the full power of single-particle LSPR.

Albeit scarce, the few existing studies have already suggested the importance of single-particle heterogeneity in LSPR. Peters et al. compared the spectral heterogeneity of different gold nanoparticle geometries by using a white-light source in conjunction with a series of narrow-band-pass filters to measure scattering intensity at multiple wavelengths in LSPR.[24] With each nanoparticle geometry exhibiting a vastly different LSPR spectral profile, they tailored the signal detection by carefully choosing the bandpass filter(s). Despite these modifications, they noticed that, for more spectrally heterogeneous nanoparticle geometries, 20% or potentially more of the particles exhibited an undetectable binding response because the illumination wavelength falls outside of the optimal range relative to the particle LSPR peak wavelengths. While offering important insights, this technique is based on wavelength scanning and therefore limited in its ability to perform rapid spectral profiling, and its intensity-based detection can be prone to optical and mechanical noises.

To overcome these limitations and more systematically investigate single-particle LSPR properties, we have developed multispectral localized surface plasmon resonance (msLSPR) to monitor the SPR spectra of individual nanoparticles in real-time across the whole field-of-view. In msLSPR, we combined broad-band, dark-field microscopy with a previously described multispectral single-molecule imaging (MSSMI)[25,26] system to capture the full spectra of light scattered by each nanoparticle. MSSMI was originally developed for imaging single fluorescent molecules with ∼0.1 nm spectral and 20−50 ms temporal resolutions.[25−31] Compared to single fluorophores, metal nanoparticles exhibit much more intense scattering and do not photobleach, which offsets the somewhat lower signal throughput in dark-field microscopy and the use of a less intense, broad-band light source in msLSPR than those of the original MSSMI.[27−31] This allowed us to perform real-time, high-throughput spectral profiling on tens of nanoparticles per field of view (FOV) with ∼0.5 nm spectral precision and 100−200 ms temporal resolution. Using this approach, we evaluated the heterogeneity in LSPR spectral and sensing properties of several gold nanoparticles, including spheres, rods, and bipyramids, that are commonly used as LSPR sensors. Simulations based on these measurements reiterate the impact of particle-to-particle heterogeneity on the signal uniformity and sensitivity of LSPR assays and demonstrate the potential advantage of performing LSPR in the spectral domain.

RESULTS AND DISCUSSION

Multispectral Localized Surface Plasmon Resonance (msLSPR) Setup. We constructed the msLSPR imaging system on a commercial, inverted microscope frame (Figure 1A) based on the MSSMI system in our previous work with significant modifications necessary for LSPR imaging.[25] In particular, dark-field illumination was achieved by coupling a halogen light source to a dark-field condenser of high numerical aperture (NA = 1.4), which transmits light at high oblique angles to the focal volume (Figure 1B). The scattered signal is collected by a 20× air objective with a lower NA (0.75), enabling a wide field-of-view acquisition at a long working distance (1 mm). The signal is then split at an ∼30:70 ratio between a positional channel and a spectral channel, respectively. The positional channel uses a regular imaging path to project the dark-field image of the FOV to half of an sCMOS detector. In the spectral channel, a prism disperses the signal into its wavelength components, which are then projected onto the other half of the detector to yield adjacent positional and spectral images.

We performed experiments using a flow cell (Figure 1C) for real-time monitoring of LSPR properties of nanoparticles, such as peak location, peak intensity, and plasmon line width (defined as the full width at half-maximum of the SPR spectrum), upon interaction with different molecules in designated buffers. A flow cell consists of a glass slide (top side in contact with dark-field condenser) and coverslip (bottom-side support) sandwich assembly. We used fire-polished borosilicate glass slides, which exhibit minimal background scattering at the imaging interface compared with conventional slides, to significantly improve the signal to background ratio. The slide surface was also treated with positively charged 3-aminopropyltriethoxysilane (APTES), and citrate-coated nanoparticles could electrostatically absorb to the slide surface at proper densities prior to imaging.

The msLSPR imaging system generates matched positional and spectral images for each light-scattering object in the FOV (Figure 1D). The pixel intensity profile of the spectral image, elongated along the direction of dispersion, encodes the scattering spectrum of the object (Figure 1E). To convert pixel-based spectral images to wavelength-based spectral profiles, we first calibrated the system in a manner similar to what was previously demonstrated.[25] Briefly, we imaged the same gold nanorods with a band-pass filter inserted in the imaging path to specify a narrow wavelength range (10−20 nm bandwidth) to be preserved in the spectral channel. As such, the spectral image of each nanoparticle is reduced to only a few pixels in the dispersion direction, and the spectral shift distance (*ssd*) at this wavelength (range) could be computed. Here, *ssd* values represent the offset between the centroid positions of the positional and spectral images of matching particles and are wavelength dependent. We aligned the instrument in such a manner that the positional and spectral images acquired using a 661 ± 5.5 nm band-pass filter coincided (i.e., *ssd* at 661 nm = 0). This wavelength was chosen because it lies near the middle of the LSPR bands for commonly used gold nanoparticles.

Next, by using band-pass filters with different center wavelengths ranging from ∼550 to ∼750 nm and measuring the corresponding *ssd* values, we obtained a calibration plot
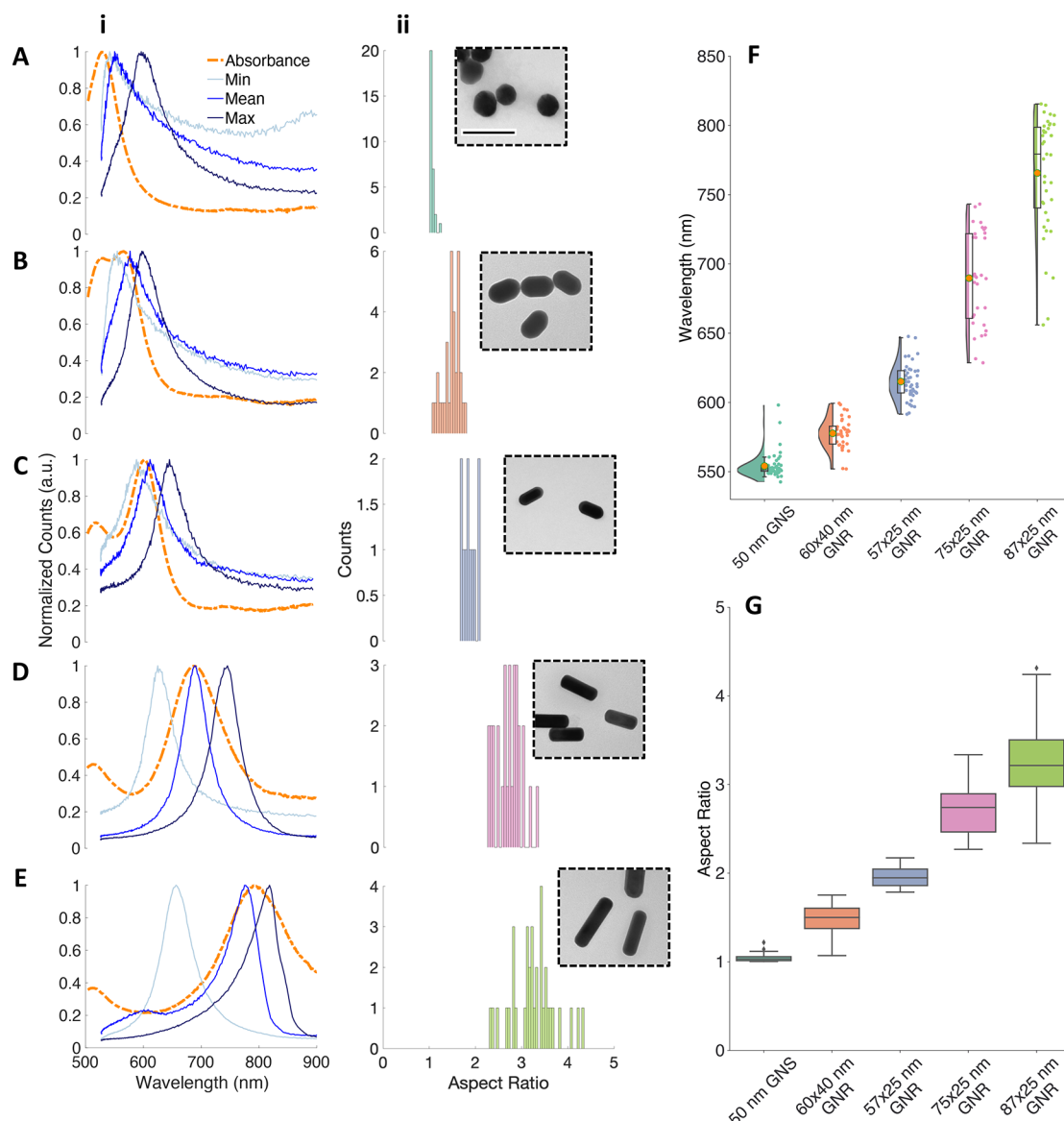
Figure 2. Measuring the LSPR heterogeneity of single gold nanospheres (GNSs) and nanorods (GNRs): (A) 50 nm GNS; (B) 60 × 40 nm GNR; (C) 57 × 25 nm GNR; (D) 75 × 25 nm GNR; (E) 87 × 25 nm (actual size 103 × 32 nm) GNR. Column i: single-particle msLSPR measurements. Thin lines display minimum, mean, and maximum LSPR peak locations. The overlaid thicker dashed line displays a separately acquired ensemble colloidal gold dispersion LSPR absorbance spectrum. Column ii: recorded aspect ratios for all nanoparticles from TEM images (inset, scale bar = 100 nm). TEM images were acquired at 120 kV. (F) Raincloud plot showing LSPR peak location density distribution and quartiles for all gold nanospheres and nanorods. (G) Box and whisker plot of all measured aspect ratios for all gold nanospheres and nanorods.

(Figure S1), which demonstrates the nonlinear relationship between the pixel position in the spectral image (i.e., *ssd*) with the absolute wavelengths. Each pixel in the spectral image is equivalent to ∼1.2 nm at short wavelengths (550−650 nm) and ∼1.7 nm at longer wavelengths (∼700 nm or above), averaging to ∼1.4 nm per pixel across the calibration range. Fitting the plot with a second-order polynomial yields an empirical formula that converts the pixel-based spectra (Figure 1E) into the corresponding, wavelength-based spectra (Figure 1F). Of note, the band-pass filters were only used for calibration and removed for msLSPR measurements unless otherwise stated.

With the complete msLSPR imaging and analysis workflow established, we examined the temporal stability of 75 × 25 nm gold nanorods sitting in blank imaging buffer over time. The strong signal from these nanorods allowed us to record the positional and spectral images at 100−200 ms temporal resolution. At an acquisition rate of 200 ms/frame, we observed highly reproducible frame-to-frame LSPR spectra with minimal fluctuations within an entire 30 min acquisition window (Figure 1G). The root mean square (RMS) for a typical LSPR peak trace was less than 0.2 nm, indicating excellent spectral stability (Figure 1H). This offered us a quality check of the msLSPR setup and assay format, providing the basis for evaluating the spectral and sensing heterogeneities of the nanoparticles based on the recorded LSPR spectra and their temporal evolutions. The observed spectral stability also confirms that the impact from the buffer or the light source (a halogen lamp with low energy density) on the LSPR properties

Table 1. Spectral, Sensing, and Morphological Properties for Each Particle Type[a]

particle type (w/vendor-specified dimensions)	av initial peak location (nm)	av plasmon line width (nm)	av SH-PEG$_{2k}$ peak shift (nm)	av measd length (nm)	av measd width (nm)	av measd aspect ratio
GNS (50 nm)	554.1 ± 9.3 (1.7% CV)	54.6 ± 11.4 (20.9% CV)	2.1 ± 0.9 (42.9% CV)	46.1 ± 3.2 (6.9% CV)	44.1 ± 3.1 (7.1% CV)	1.1 ± 0.1 (9.1% CV)
	$N = 49$	$N = 49$	$N = 21$	$N = 30$	$N = 30$	$N = 30$
	$(\lambda_{\mathrm{msLSPR}} - \lambda_{\mathrm{abs}} = 25.1$ nm)					
GNR (60 × 40 nm)	577.7 ± 11.1 (1.9% CV)	61.7 ± 5.7 (9.2% CV)	2.7 ± 0.7 (25.8% CV)	59.1 ± 8.7 (14.8% CV)	40.1 ± 2.8 (7.1% CV)	1.5 ± 0.2 (13.3%CV)
	$N = 36$	$N = 36$	$N = 18$	$N = 33$	$N = 33$	$N = 33$
	$(\lambda_{\mathrm{msLSPR}} - \lambda_{\mathrm{abs}} = 12.7$ nm)					
GNR (57 × 25 nm)	615.1 ± 12.9 (2.1% CV)	58.7 ± 3.5 (5.9% CV)	4.5 ± 0.9 (20.0% CV)	50.9 ± 4.7 (9.3% CV)	26.0 ± 1.7 (6.6% CV)	2.0 ± 0.1 (5.0% CV)
	$N = 44$	$N = 44$	$N = 26$	$N = 21$	$N = 21$	$N = 21$
	$(\lambda_{\mathrm{msLSPR}} - \lambda_{\mathrm{abs}} = 11.1$ nm)					
GNR (75 × 25 nm)	689.8 ± 34.0 (4.9% CV)	56.5 ± 2.5 (4.5% CV)	6.2 ± 0.8 (12.9% CV)	75.0 ± 6.3 (8.4% CV)	27.8 ± 1.2 (4.4% CV)	2.7 ± 0.3 (11.1%CV)
	$N = 32$	$N = 32$	$N = 16$	$N = 29$	$N = 29$	$N = 29$
	$(\lambda_{\mathrm{msLSPR}} - \lambda_{\mathrm{abs}} = 0.8$ nm)					
GNR (87 × 25 nm)	765.7 ± 42.6 (5.6% CV)	64.5 ± 6.3 (9.8% CV)	3.5 ± 1.2 (34.3% CV)	103.3 ± 11.3 (10.9%CV)	32.0 ± 2.9 (9.0% CV)	3.3 ± 0.5 (15.2%CV)
	$N = 39$	$N = 39$	$N = 9$	$N = 35$	$N = 35$	$N = 35$
	$(\lambda_{\mathrm{msLSPR}} - \lambda_{\mathrm{abs}} = -29.3$ nm)					
GNBP (105 × 35 nm)	778.3 ± 33.8 (4.3% CV)	63.9 ± 5.0 (7.8% CV)	9.2 ± 0.9 (9.8%CV)	96.8 ± 2.4 (2.5% CV)	32.7 ± 1.4 (4.4% CV)	3.0 ± 0.1 (3.3% CV)
	$N = 12$	$N = 12$	$N = 12$	$N = 25$	$N = 25$	$N = 25$
	$(\lambda_{\mathrm{msLSPR}} - \lambda_{\mathrm{abs}} = -8.7$ nm)					
GNBP (100 × 30 mn nm)	754.4 ± 26.9 (3.6% CV)	66.9 ± 6.0 (9.0% CV)	10.2 ± 1.6 (15.7% CV)	77.3 ± 7.5 (9.7% CV)	29.8 ± 3.5 (11.6% CV)	2.6 ± 0.4 (15.4%CV)
	$N = 64$	$N = 64$	$N = 11$	$N = 40$	$N = 40$	$N = 40$
	$(\lambda_{\mathrm{msLSPR}} - \lambda_{\mathrm{abs}} = -0.2$ nm)					
aged GNBP (100 × 30 nm)*	806.5 ± 20.0 (2.5% CV)	77.4 ± 9.3 (12.0% CV)	3.7 ± 4.0 (108.1% CV)	125.9 ± 6.8 (5.4% CV)	42.8 ± 3.4 (7.9% CV)	3.0 ± 0.2 (6.7% CV)
	$N = 37$	$N = 37$	$N = 8$	$N = 64$	$N = 64$	$N = 64$
	$(\lambda_{\mathrm{msLSPR}} - \lambda_{\mathrm{abs}} = -10.5$ nm)					

[a]The average value, standard deviation, and percent coefficient of variation (% CV) are shown for the single-particle data. Lengths, widths, and aspect ratios were collected for morphologically intact nanoparticles.

of the particles was minimal, at least on the time scale of our experiments.

LSPR Heterogeneity of Single Gold Nanospheres and Nanorods. With the performance of msLSPR validated, we were able to rapidly profile spectral variations among individual nanoparticles that are often obscured in ensemble measurements. We initially focused on gold nanospheres (GNSs) and nanorods (GNRs) because they represent the most common plasmonic particle geometries utilized in LSPR sensing. Similar to that done in Figure 1, we obtained single-particle measurements by immobilizing nanoparticle solutions in the flow cell and acquiring spectra for all of the nanoparticles within the FOV. To avoid potential interactions or signal crosstalk among the nanoparticles, we immobilized not more than 20 nanoparticles per FOV and imaged multiple FOVs to obtain data for a sufficient number (typically 20−60) of particles under each experimental condition.

We performed msLSPR measurements for a 50 nm (diameter) GNS and four different sizes of GNRs: 60 × 40, 57 × 25, 75 × 25, and 87 × 25 nm. The solid blue lines in the left panels (panels (i) of Figure 2A−E) correspond to

representative single-particle LSPR spectra obtained at 200 ms exposure time within the 530−900 nm wavelength range on the msLSPR, highlighting the extent of variations in both the peak locations $(\lambda_{\mathrm{LSPR}})$ and spectral shapes for each particle type. Our measurements revealed large spectral variations for GNS and GNR. While most 50 nm GNS had LSPR peaks at around 554.1 ± 9.3 nm (standard deviation, the same hereafter), a small fraction of GNS particles had significantly red-shifted LSPR spectra peaking above 550 nm. Even greater variations were observed on GNRs, and the spectral heterogeneity increased with particle length. In the case of 87 × 25 nm GNRs, the LSPR peaked within the whole range from ∼660 to ∼840 nm, averaging 765.7 (±42.6) nm. A comprehensive list of the LSPR measurements is presented in Table 1. The red dashed lines in the same panels display the ensemble colloidal gold dispersion absorbance spectra of the particles for comparison. The comparison shows that our single-particle λ_{LSPR} measurements largely recapitulated ensemble colloidal gold dispersion absorbance data except for the 50 nm GNS due to LSPR cutoff below 530 nm. The agreement could be even better if more (e.g., hundreds of)
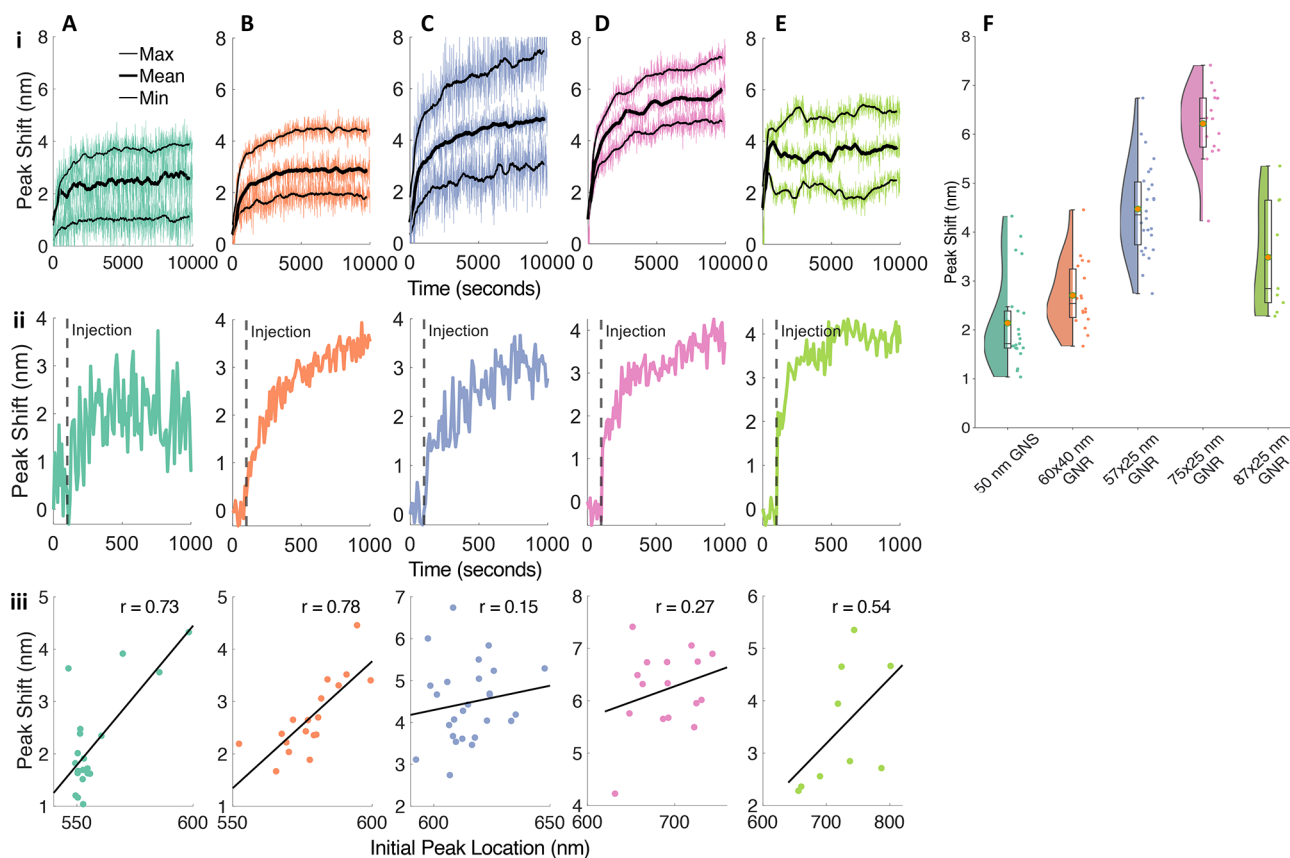
Figure 3. Single-particle msLSPR sensing with gold nanospheres (GNSs) and nanorods (GNRs): (A) 50 nm GNS; (B) 60 × 40 nm GNR; (C) 57 × 25 nm GNR; (D) 75 × 25 nm GNR; (E) 87 × 25 nm (actual size 103 × 32 nm) GNR. Row i: LSPR peak shift time traces of 1 mM of thiol-containing polyethylene glycol with molecular weight M_w = 2 kDa (SH-PEG$_{2k}$) grafting onto the nanoparticle surface. The individual traces highlight representative nanoparticles that display the minimum, mean, and maximum peak shift after the full acquisition window. Each time trace consists of an acquisition window of 10000 s with a 10 s interval between each 200 ms exposure frame. Row ii: LSPR peak shift time traces of 1 mM of thiol-containing polyethylene glycol with molecular weight M_w = 2 kDa (SH-PEG$_{2k}$) grafting onto a representative nanoparticle surface. Each time trace consists of the first 1000 s and highlights the time of injection (vertical line at t = 100 s). Row iii: scatterplots of initial peak location vs final peak shift (difference between t = 100 and t = 10000 s) for all individual nanoparticles. A linear regression is fitted to each scatterplot as a guide in highlighting the presence or lack thereof of correlation. (F) Raincloud plot showing LSPR final peak shift (t = 10000 s) density distribution and quartiles for all gold nanospheres and nanorods.

nanoparticles were analyzed. It needs to be noted, however, that msLSPR measures scattering, whereas the ensemble spectra measure total extinction (both absorption and scattering). In all cases, it was also evident that single-particle LSPR spectra were much narrower than the ensemble colloidal gold dispersion absorbance spectra, which is somewhat expected, since the latter reflect the summed LSPR spectra of all particles in solution.

Using transmission electron microscopy (TEM), we found that the observed spectral variations for each particle type were well paralleled by the variations in particle morphology. TEM images in panels (ii) of Figure 2A−E provided us with length and width information, which we then used to calculate aspect ratios (ARs). In general, the GNRs had higher variations in AR compared to the GNSs. For most of the geometries, the measured dimensions are close to those specified by the vendor. The 87 × 25 nm GNR, however, displayed dimensions (103 × 32 nm) much larger than specified, resulting in a surface area that is roughly 1.5× that expected. The similarities in dimensional and spectral variations became apparent when examining Figures 2F,G, which highlight the density distribution and quartiles for the LSPR peak location measurements and the histograms for AR for each particle,

respectively. This similarity indicates that the observed heterogeneity in λ_{LSPR} for both the GNRs and the GNSs could largely be attributed to heterogeneity in particle morphology. These morphological differences arise from the nucleation and growth mechanism of the nanoparticles. Gold nanorods grow from single-crystalline seeds, and they exhibit {100} top facets and eight side facets inequivalent to the top facets.[32] During synthesis, variations in local growth conditions can lead to varying side facet growth rates, which directly affect the aspect ratio.[33−35]

The morphological variations in these nanoparticles could lead to heterogeneities in the LSPR peak positions, as reported above and by others,[24] the plasmon line width,[36] and potentially also the sensitivity of the LSPR signal to ligand binding. The plasmon line width reflects the spectral shape and is related to the size of the nanoparticle through radiative damping.[37,38] The observed variations in spectral line widths (see Table 1) in these particles therefore corroborate the role of particle morphological variations (as observed in the TEM images) in LSPR spectral heterogeneity of the particles. Like its spectral profile, the LSPR sensitivity of a particle could also depend on the particle structure and morphological characteristics and be heterogeneous for populations of nanoparticles
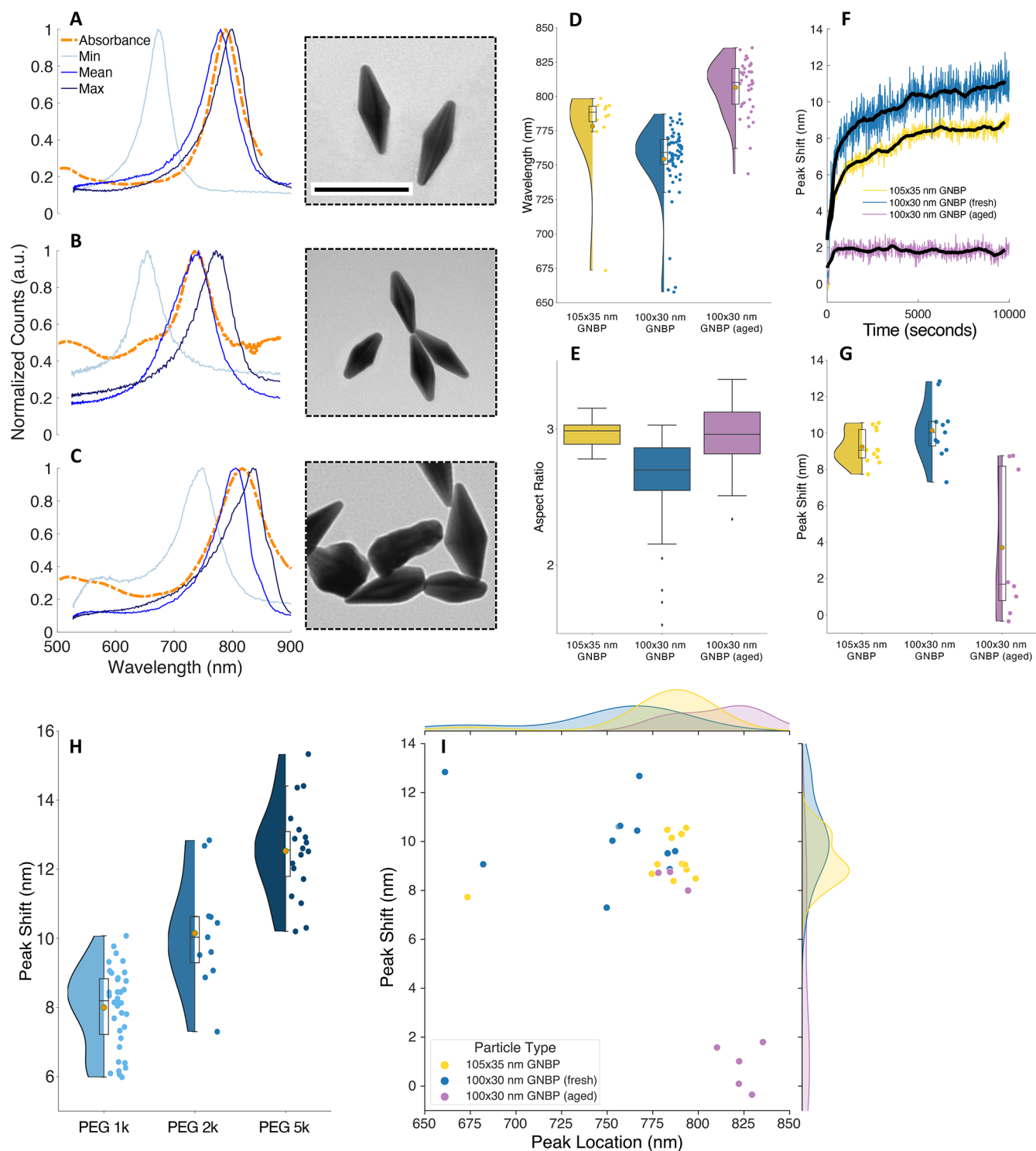
Figure 4. Measuring the spectral and sensing heterogeneity of single gold nanobipyramids (GNBPs) with msLSPR: (A) 105 × 35 nm GNBP, (B) 100 × 30 nm GNBP, and (C) 100 × 30 nm GNBP aged 4 months after their expiration date. The left panels in (A)−(C) show single-particle msLSPR measurements: thin lines display minimum, mean, and maximum LSPR peak locations. The overlaid thicker dashed line displays a separately acquired ensemble colloidal gold dispersion LSPR absorbance spectrum. The right panels in (A)−(C) show TEM images (scale bar: 100 nm) for each GNBP type acquired at 120 kV. (D) Raincloud plot showing LSPR peak location density distribution and quartiles for all gold nanobipyramids. (E) Box and whisker plot of measured aspect ratios for all gold nanobipyramids. (F) LSPR peak shift time traces of 1 mM thiol-containing polyethylene glycol with molecular weight M_w = 2 kDa (SH-PEG$_{2k}$) grafting onto the nanoparticle surface. Each GNBP type is represented by a nanoparticle that displays the mean peak shift after the full acquisition window. Each time trace consists of an acquisition window of 10000 s with a 10 s interval between each 200 ms exposure frame. (G) Raincloud plot showing LSPR peak shift density distribution and quartiles for all tested gold nanobipyramids. (H) Raincloud plot showing 100 × 30 nm GNBP LSPR peak shift density distribution and quartiles for 1 mM thiol-containing polyethylene glycol with molecular weights M_w = 1, 2, and 5 kDa. (I) Joint plot displaying initial peak location vs final peak shift (t = 10000 s) for all individual GNBPs.

with nonuniform morphology. However, the sensing heterogeneity of gold nanoparticles and, in particular, how the initial LSPR peak position is correlated with the sensing response, has not been systematically investigated at the spectral resolution achieved with the msLSPR. We therefore set out to address this question next.

Single-Particle SH-PEG$_{2k}$ Sensing on GNS and GNR. With the ability to monitor the LSPR spectrum of individual NPs in a wide-field setting, we next sought to assess the single-particle LSPR sensitivity. We profiled the same five GNS and GNR geometries investigated above by recording single-particle time traces of λ_{LSPR} shift as the nanoparticles were grafted with thiol-containing polyethylene glycol (SH-PEG$_{2k}$, M_w = 2 kDa). These traces are shown in panels (i) of Figure 3A−E. SH-PEG$_{2k}$ is an excellent moiety to study λ_{LSPR} shift because it reliably grafts onto gold nanoparticles as compact self-assembled monolayers.[39−41] For these experiments, the SH-PEG$_{2k}$ solution was gently flown into the sample cell using a syringe pump at t = 100 s, and the LSPR spectrum of each particle was monitored in real time to record the sensing process as SH-PEG$_{2k}$ was installed on the gold surfaces over 10000 s (∼3 h). These traces allowed us to evaluate not only the sensitivity of each particle (as the total λ_{LSPR} shift) but also the potential association between the sensitivity and the initial λ_{LSPR} of each particle type.

A comparison of the LSPR sensitivities among all the nanoparticle geometries is presented in Figure 3F. Of all the particles, the 50 nm GNS experienced the lowest average λ_{LSPR} shift of 2.1 ± 0.9 nm while simultaneously having the highest variance (42.9% CV, where CV is the coefficient of variation). This is in accordance with previous reports suggesting that spheres exhibit the lowest LSPR sensitivity due to their lack of sharp corners and edges.[42] The 75 × 25 nm GNR experienced the highest average λ_{LSPR} shift of 6.2 ± 0.8 nm accompanied by the lowest variance (12.9% CV), evoking the strongest and most homogeneous response among all the nanorods tested. While some simulations have indicated that smaller nanorods (such as the 57 × 25 nm GNR) may be more optimal sensors,[17] our work corroborates a previous piece of literature indicating that GNRs with AR ≈ 3 are the most optimal.[16] We could relate the LSPR sensitivity readouts again to particle morphology. The GNR width (diameter) reflects the size of the hot-spot regions, where high variance of this dimension could lead to a high variance in the λ_{LSPR} shift upon analyte binding.[20,43] The 75 × 25 nm GNRs displayed the lowest morphological width variance (4.4% CV; see Figure 1 and Table 1) and the highest LSPR shift. In general, GNRs with larger aspect ratios tended to have larger average λ_{LSPR} shifts and smaller λ_{LSPR} shift variances. The 87 × 25 nm (actual size 103 × 32 nm by TEM) GNR was an exception to this trend, displaying a λ_{LSPR} shift of 3.5 ± 1.2 nm (34.3% CV) comparable to that of the 60 × 40 nm GNRs. We can surmise that the lower λ_{LSPR} shift sensitivity of this GNR is due to the noticeably larger width (32 nm) compared to the other two GNRs (∼25 nm), indicating that the nanorod width could have a strong impact on the λ_{LSPR} shift sensitivity. In addition, we noticed that the most sensitive 75 × 25 nm GNRs exhibited the most uniform plasmon line widths (4.5% CV; see Table 1) while the least sensitive 50 nm GNS exhibited the least uniform plasmon line widths (20.9% CV; see Table 1). Thus, the plasmon line width, in addition to LSPR peak location and morphology measurements, together paint a consistent picture in predicting LSPR sensitivity on a per-particle basis.

Since msLSPR monitors the full scattering spectra of individual nanoparticles in real time, we were also able to assess potential correlations between the initial λ_{LSPR} and the LSPR response for each particle. The 50 nm GNS and 60 × 40 nm GNR exhibited moderately strong correlation values of 0.73 and 0.78, respectively, while the other three GNR dimensions showed no moderate or strong correlation (panels iii, Figure 3A−E). The LSPR peak location is highly dependent on nanoparticle size, while the LSPR peak shift is highly dependent on the grafting of the hot-spot regions. For GNR, those hot-spot regions belong to the end-cap portions of the NP.[43] As the aspect ratio increases, the relative contribution from the hot-spot regions remains relatively unchanged and thus the sensitivity does not depend largely on the initial peak location. Nevertheless, we found pairs of nanoparticles that showed similar peak locations but highly different peak shifts (Figure S2). These pairs are rare, but they highlight the need to characterize the entire nanoparticle population's LSPR characteristics. We also note that in some cases the sensing traces showed an initial increase followed by a slight decrease in peak shift during incubation, potentially due to the long-term rearrangement of the PEG layer after an initial, fast absorption process (Figure 3E).

Spectral and Sensing Heterogeneity of Single Gold Nanobipyramids (GNBPs). Although gold nanorods have been employed as individual plasmonic sensors, gold nano-bipyramids (GNBPs) are attracting interest due to their increased sensitivity to local refractive index changes and homogeneous response to analyte binding. A previous study by Peters and colleagues discovered a strong reduction in aspect ratio heterogeneity, which enabled a more homogeneous response to antibody incubation in comparison with gold nanorods.[24] Their imaging setup consisted of a white-light source in conjunction with narrow-band-pass filter(s) to image scattered intensity at chosen wavelengths of the LSPR. Intensity changes induced by analyte binding strongly depend on the probe wavelength relative to the average LSPR peak wavelength. Using this technique, a wide distribution of individual LSPR peak locations can be difficult to resolve and even impossible to resolve if the probe wavelength directly overlaps with the plasmon resonance. With msLSPR, we are able to probe all nanoparticles in the FOV with sufficient signal and we hypothesize that it is necessary to resolve and monitor the LSPR spectra of all individual NPs. We demonstrate that despite spectral heterogeneities within GNBP populations, the LSPR responses were more uniform than those observed for the GNS and GNR. Finally, we show that GNBP sensing performance depends on morphology intactness rather than on homogeneity of the aspect ratios.

We performed msLSPR measurements on GNBPs from two slightly different geometries: namely, 105 × 35 nm (Nano-Seedz) and 100 × 30 nm (Nanopartz). These selected geometries display sufficient light-scattering signals compared to GNBPs with smaller dimensions. The observed λ_{LSPR} values were 778.3 ± 33.8 nm (% CV = 4.3) and 754.4 ± 26.9 nm (% CV = 3.6) for the NanoSeedz and Nanopartz GNBPs, respectively (Figure 4A,B, left panels), in agreement with ensemble colloidal gold dispersion absorbance data (red dashed lines in the same panels). These measurements show that the spectral variations of GNBPs, at least in the geometries tested here, are not any lower than those of the other nanoparticles tested earlier in terms of %CV or absolute wavelength. TEM imaging (Figure 4A,B, right panels)
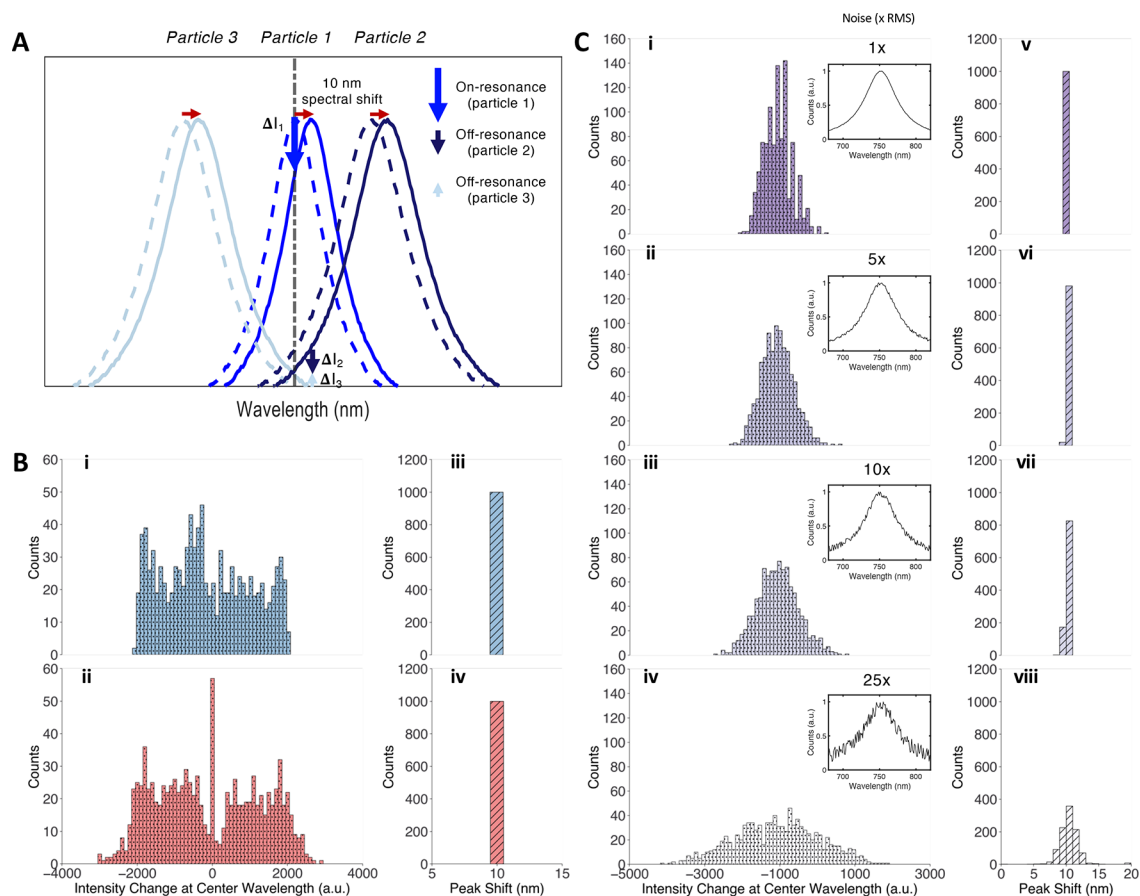
Figure 5. Simulating the advantages of msLSPR sensing compared to conventional intensity-based measurements. (A) 1000 randomly distributed replicates of gold nanorods and nanobipyramids generated with peak location and plasmon line width information derived from earlier measurements. A 10 nm spectral red shift is induced for all nanoparticles. In the schematic, 3 representative nanoparticles exhibiting vastly different LSPR peak locations are highlighted. Intensity changes are calculated for each nanoparticle at the center illumination wavelength (dashed gray line) before (dashed blue line) and after spectral shift (solid blue line), resulting in a nonuniform sensing signal. **(B)** In populations of GNR ((i), (iii)) and GNBP ((ii), (iv)) with normally distributed LSPR peak positions, spectral detection ((iii), (iv)) can reliably recover the 10 nm LSPR peak shift, whereas intensity detection ((i), (ii)) has a nonuniform response. **(C)** In populations of GNBP with homogeneous peak locations, varying levels of msLSPR system noise ((i), (v), 1×; (ii), (vi), 5×; (iii), (vii), 10×; (iv), (viii), 25×) were applied and then measured by intensity ((i)−(iv)) or peak location change ((v)−(viii)).

indicated that the Nanopartz (100 × 30 nm) GNBPs had among the highest length (9.7% CV) variance and the absolute highest width (11.6% CV) variance among all the particles tested. In contrast, the NanoSeedz (105 × 35 nm) GNBPs have the lowest length (2.5% CV) and width variance (4.4% CV) among all geometries tested. This dichotomy continued for the aspect ratios (Figure 4E), where the Nanopartz particles exhibited the highest variance (15.4% CV) among all particles while the NanoSeedz particles exhibited the lowest variance (3.3% CV).

Despite the apparent spectral and geometrical heterogeneities of these GNBPs, the recorded LSPR peak shifts upon SH-PEG$_{2k}$ absorption were much higher and more uniform compared with those observed earlier on GNRs and GNSs. This is evident from Figure 4F,G, where both types of GNBPs consistently showed LSPR peak shifts >8 nm (9.2 ± 0.9 nm (9.8% CV) and 10.2 ± 1.6 nm (15.7% CV) for the NanoSeedz and Nanopartz GNBPs, respectively).

We have also examined the effect of the size of the grafted molecules on the shifting response using the Nanopartz GNBPs. To this end, we compared the sensing response of the GNBPs among three different sizes of SH-PEGs: namely, PEG$_{1k}$, PEG$_{2k}$, and PEG$_{5k}$. As shown in Figure 4H, we

observed a uniform and size-dependent LSPR peak shift (8.0 ± 1.2 nm (14.5% CV) and 12.5 ± 1.4 nm (11.2% CV) for SH-PEG$_{1k}$ and SH-PEG$_{5k}$, respectively). At least within the range tested here, SH-PEG molecules with longer PEG chains caused stronger LSPR responses. This result confirms the uniformity of GNBP sensitivity and highlights the impact of the immediate environment on the observed LSPR properties.

We noticed that in certain circumstances GNBPs (100 × 30 nm aged) could lose their sharp edges and, correspondingly, their LSPR sensitivity (3.7 ± 4.0 nm). These particles exhibited two distinct spectral and sensing clusters (Figure 4I). The particles that responded to SH-PEG grafting showed an average λ_{LSPR} of 785 nm, while the particles that did not respond to SH-PEG grafting showed an average λ_{LSPR} of 824 nm. A noticeable λ_{LSPR} red shift can be indicative of nanoparticle deterioration, as shown through TEM imaging of the aged GNBPs. Hence, for GNBPs, the sensing performance primarily depends on the structural intactness (i.e., well-preserved sharp edges) and much less so on the uniformity of the aspect ratios. Our results demonstrate the power of resolving and monitoring LSPR spectra of individual NPs.

Advantages of msLSPR in Overcoming Particle Heterogeneity for Molecular Sensing. The observed LSPR heterogeneity on both GNRs and GNBPs could have significant implications in molecular sensing. To date, most SPR-based sensing relies on intensity readout upon illumination with narrow-band light sources. Despite reports of sensitivity down to single molecules, intensity-based LSPR sensing is susceptible to heterogeneities among the nanoparticles. Specifically, only a fraction of the nanoparticles will be on-resonance and exhibit high SPR response upon ligand binding, leading to a nonuniform sensing signal (Figure 5A). This issue can be entirely avoided with msLSPR, with which a signal is detected in the spectral domain, as shown by the simulations described below.

For the simulations, we first created 1000 randomly distributed replicates of GNR and GNBP spectra with peak locations and plasmon line widths derived from earlier measurements. We then artificially induced a 10 nm red shift in the LSPR spectra of all nanoparticles, assuming that all nanoparticles exhibit a uniform response (in shifting their LSPR spectra) upon ligand binding. We chose to use this uniform spectral shift to simplify the simulations. Next, for intensity-based LSPR measurements, we calculated the intensity changes for each nanoparticle at the center illumination wavelength before and after ligand binding. The spectral detection was performed in a manner similar to that demonstrated earlier in this work. With this workflow, we were able to compare side by side the performance of spectral (broad-band msLSPR) vs fixed-wavelength intensity measurements.

The simulations show that spectral detection, as opposed to intensity detection, can reliably recover LSPR spectra regardless of their peak location (Figure 5B). In a simplified scenario where a uniform shift is induced, spectral detection accurately measured the LSPR peak shift, whereas intensity-based measurements yielded a distribution. In populations of both GNR (Figure 5B, panel (i)) and GNBP (Figure 5, panel (ii)) with normally distributed LSPR peak positions, a small subset of NPs had an optimal response to ligand binding. This subpopulation of nanoparticles was slightly off-resonance, typically 10−20 nm away from the center wavelength (Figure S3). Outside of this range, the signal declined sharply, and most of the nanoparticles exhibited a suboptimal response. Ligand-induced signals essentially diminished on a significant fraction of nanoparticles that were entirely off-resonance with the light source. These nanoparticles displayed insufficient intensities to be initially detected. In contrast, we observed a consistent 10 nm peak shift readout on the same nanoparticles with spectral (msLSPR) detection ((iii) and (iv)). Although the simulations were based on a uniform, 10 nm spectral shift, msLSPR is expected to accurately detect spectral shifts in other amplitudes as well, provided there is sufficient signal to noise in imaging. Thus, in real-world samples (where the nanoparticles are heterogeneous in geometry) and measurement settings (each nanoparticle is situated in a somewhat different environment), spectral detection such as that based on msLSPR offers a much more accurate response than the current, intensity-based approaches.

The simulations further revealed that msLSPR is also much more resistant to measurement noise than intensity-based measurements. Like any other imaging-based assays, single-particle LSPR measurements can be prone to optical and mechanical noise. In Figure 5C, we simulated a homogeneous GNBP population (LSPR peak locations 744−758 nm) with varying levels of noise (also experimentally derived), and ligand-induced intensity or spectral shifts were similarly analyzed as above. We noticed again that a subpopulation of NPs displayed insufficient signals despite the homogeneous distribution of peak locations, reinforcing the concept that intensity-based measurements rely on signal contrast and an optimal distribution of peak locations to be effective. Upon increasing the noise levels to 5×, 10×, and 25× that normally seen on our imaging system (Figure 5C, panels (i)−(iv)), we observed a broadened distribution of intensity readouts (34.8% CV at 1× noise, 40.0% CV at 5×, 51.6% CV at 10×, and 104.2% CV at 25×), further confounding an already nonuniform response. With spectral detection (panels (v)−(viii)), however, we observed a constant response in average spectral shift at 10 nm, and the signal varied minimally at up to 10× the noise level (0% CV at 1× noise, 1.6% CV at 5×, 5.3% CV at 10×). Even at 25× the noise level, msLSPR showed only 15.7% CV in signal variation, further demonstrating the robustness of msLSPR in quantitative assays.

These simulations demonstrate the potential advantages of msLSPR (and alternative spectral detection strategies) over conventional intensity-based detection in quantitative LSPR sensing. The results clearly suggest that, in an intensity-based LSPR experiment, both nanoparticle homogeneity and a proper choice of the excitation wavelength are key to achieving optimal performance. It can be challenging to meet both criteria in all experimental settings (e.g., when using different types of nanoparticles). In contrast, msLSPR spectral detection can accurately profile all nanoparticles with no concerns regarding peak position heterogeneity. Furthermore, we demonstrated the superior noise tolerance of msLSPR, which may also help deliver better sensitivity in actual sensing applications.

CONCLUSIONS

We have demonstrated msLSPR, a wide-field, multispectral imaging platform capable of profiling many single nanoparticles in parallel with high spectral and temporal resolutions. With msLSPR, we analyzed light scattering properties of individual gold nanospheres, nanorods, and nanobipyramids under broad-band illumination. The results allowed us to examine the spectral and sensing properties of the different nanoparticle geometries and assess the potential connection between the two properties. Our analysis revealed heterogeneities in both properties in all nanoparticles tested, but different geometries exhibited widely varying degrees of heterogeneities. The association between the initial LSPR peak position and the sensing performance also depends on the particle type and geometry. Simulations based on the experimental observations suggest that, compared with conventional SPR assays based on measuring change in scattering intensity, measurements in the spectral domain such as by using msLSPR have potential advantages in overcoming particle-to-particle heterogeneities. In addition to examining LSPR heterogeneities as presented here, being able to monitor the full scattering spectrum of a large number of nanoparticles in parallel will be instrumental in studying LSPR for both theoretical investigations and assay development. As we have previously demonstrated, the dual-channel configuration of MSSMI allows imaging of particles in motion without compromising spectral resolution.[25] We expect msLSPR to be similarly capable of analyzing nanoparticles in

suspension (thus in motion), which will further expand the types of samples compatible with msLSPR and make the msLSPR a broadly useful tool for plasmonics-based biosensing.

METHODS

Microscopy. The custom multispectral localized surface plasmon resonance (msLSPR) imaging system was constructed with modifications based on previous work.[25] Dark-field illumination was achieved by coupling a halogen lamp (wavelength range 400−1000 nm) with an aluminum reflector (L1090, International Light Technologies, and DC950H illuminator, Dolan-Jenner) to a CytoViva high-resolution dark-field condenser. The scattered signal was collected at the side port of an inverted Nikon Eclipse TE2000-U microscope frame equipped with a 20× air objective (Nikon, NA 0.75). A slit (VA100, Thorlabs) was placed at the intermediate image plane to narrow the field of view. The signal was focused through a triplet lens (PAC076, Newport; f = 125 mm) onto a nonpolarizing beam splitter (BS022, Thorlabs), which divided the signal into positional (30%, transmitted) and spectral (70%, reflected) channels. The signal in each channel was refocused with another triplet lens (f = 125 mm) before the two channels were combined using a knife-edge mirror (MRAK25-E02, Thorlabs) and projected onto the left and right halves of the same scientific complementary metal oxide semiconductor (sCMOS) detector (ORCA-Flash 4.0 v2, Hamamatsu). To disperse the signal in the spectral channel, an equilateral prism (PS863, Thorlabs) was placed after the beam splitter and at the Fourier plane of the last focusing (triplet) lens.

Spectral Calibration. Spectral calibration of the multispectral localized surface plasmon resonance (msLSPR) imaging system was performed in a manner similar to what was previously demonstrated.[25] Gold nanorods of 75 nm length and 25 nm diameter (A12-25-700, Nanopartz) exhibiting an LSPR resonance at ∼700 nm were imaged. Narrow-band-pass filters were inserted in the infinity space below the objective to specify narrow wavelength ranges in the spectral channel. This allowed for precise calculation of centroid distance between both channels for each light-scattering object. The band-pass filters used for this purpose were all from Semrock, with part numbers FF01-572/15, FF01-605/15, FF01-635/18, FF01-661/11, FF01-673/11, FF01-711/25, and LD01-785/10. The instrument was aligned in such a manner that the positional and spectral images acquired using the FF01-661/11 filter coincided. This same filter was also used before each imaging session to obtain a registration matrix between the positional and spectral images to correct for spatial distortion across the field of view. The FF01-661/11 filter was used to register paired positional and spectral images at the other filter wavelengths and obtain mean and standard deviation measurements for the ssd values for at least 16 nanorods in the field of view. A second-order polynomial was then fit to the calibration curve, and the resulting formula allowed for conversion of ssd values from pixels to wavelength units.

Data Acquisition and Analysis. To acquire nanoparticle scattering spectra during an experiment, no filters were inserted in the infinity space below the objective in order to display full spectral dispersions in the spectral channel. Acquisitions of raw images were performed using an open-source micromanager software suite (https://micro-manager.org/).[44] Image analyses for centroid localization, spectral profiling, and temporal trajectory analysis were all performed with custom MATLAB (MathWorks) scripts as described previously.[45,46] Simulations were also performed using custom MATLAB scripts.

For spectral analysis, individual light-scattering nanoparticles were first identified in the positional channel. A corresponding center pixel position for each nanoparticle in the spectral channel was computed based on a registration matrix taken with the FF01-661/11 band-pass filter. Thus, the center pixel position in the spectral channel generated by the registration matrix corresponds to the 661 nm wavelength position. For each identified nanoparticle, a 401 pixel (rounded center position ±200 along the dispersion direction) × 15 pixel (orthogonal direction) region in the spectral image was extracted as its raw spectrum. The raw spectrum was first corrected for half-pixel spectral rounding and then shortened to a range of 20−100 pixels centered around the maximum LSPR peak location and tailored to each nanoparticle subpopulations' LSPR peak width. For each frame within an image acquisition, the spectrum was fit to a third-degree polynomial with 10 times the number of points as the pixel range. A typical image acquisition consisted of 1000 frames with a 200 ms exposure time and a 10 s interval. Spectral properties such as wavelength peak position, peak intensity, and plasmon line width were extrapolated and plotted over time, and the pixel values were subsequently converted to wavelength units using the aforementioned second-order polynomial formula.

Flow Cell Construction. The flow cell was constructed by a method similar to that previously described.[47] Fire-polished borosilicate glass slides (1025087, Applied Microarrays) were drilled with a 3/4 mm Dremel drill bit to provide lengthwise pairs of holes. Fire-polished borosilicate glass coverslips (1472313, Applied Micro-arrays) and the drilled glass slides were cleaned with sonication in 18.2 MΩ cm (at 25 °C) Milli-Q water, acetone (A949-4, Fisher Scientific), and 1% Triton X-100 detergent (T8787, Sigma-Aldrich). The glass surfaces were then incubated with a 10.7 M potassium hydroxide (KOH) (P250-50,; Fisher Scientific) for 20 min, rinsed copiously, and incubated with 3% (v/v) 3-aminopropyltriethoxysilane (APTES) (A0439, TCI Chemicals) solution in methanol (A452-4, Fisher Scientific) for 30 min. After incubation, the glass surfaces were nitrogen-dried and assembled using adhesive transfer tape (468MP, 3M) constructed to form two flow cell channels per glass slide and coverslip combination. Inlet and outlet functionalities were constructed by epoxying (20845, Devcon) Teflon tubing (TT-26, Weico Wire & Cable Inc.) to pipette tips fitted to the drill holes. Flow was incorporated into the system through a syringe pump (788110, KD Scientific) set to withdraw at 400 μL/min.

Reagents (NPs, Buffers, PEG2k). Commercial nanoparticle solutions were purchased with a negatively charged native citrate surface coating. Their part numbers are as follows: EM.GC50/4, BBI Solutions; A12-40-550, Nanopartz; A12-25-600, Nanopartz; A12-25-700, Nanopartz; A12-25-780, Nanopartz; A1B-30-780, Nanopartz; NBP-35-785-20, NanoSeedz. The deliberately aged A1B-30-780 Nanopartz bipyramids were imaged 2 months after their stated expiration date. The separately aged A1B-30-780 Nanopartz bipyramids were imaged 4 months after their stated expiration date. The nanoparticles were diluted in UltraPure DNase/RNase-Free distilled water (10977015,Thermo Fisher Scientific) to provide a surface density of approximately 20 nanoparticles per FOV. The mPEG-thiol (M_W = 2000 Da) (MPEG-SH-2000,Laysan Bio) solutions were dissolved and diluted in UltraPure water to 1 mM concentrations and filtered with a 0.1 μm filter (SLVVR33RS, Millipore) before pumping into the flow cell.

Absorbance Measurements. Absorbance measurements were performed on a Tecan Spark 20 M plate reader system. Data were acquired using the SparkControl software. Samples were typically prepared by pipetting 200 μL NP colloidal dispersions onto a 96-well plate (3632, Corning). Measurements were taken in absorbance mode for a wavelength range of 500−900 nm with a 1 nm wavelength step size.

Transmission Electron Microscopy (TEM). Transmission electron microscopy (TEM) was performed at 120 kV on a FEI Tecnai Spirit TEM system. Images were acquired using the AMT software interface on a NanoSprint12S-B cMOS camera system. TEM samples were typically prepared by drop-casting 5 μL NP colloidal dispersions in water onto 400 mesh copper TEM grids with carbon films (CF400-Cu, Electron Microscopy Sciences). The samples were allowed to air-dry for 30 min and kept overnight in a grid storage box (71150, Electron Microscopy Sciences) until the imaging time.

ASSOCIATED CONTENT

ⓈＩ Supporting Information

The Supporting Information is available free of charge at https://pubs.acs.org/doi/10.1021/acsnano.2c08702.

Information on spectral calibration for the msLSPR system, paired initial peak position and peak shift data from nanospheres and nanorods, and simulated intensity and spectral shift data (PDF)

AUTHOR INFORMATION

Corresponding Author

Xiaolin Nan − *Knight Cancer Early Detection Advanced Research Center, Oregon Health & Science University, Portland, Oregon 97201, United States; Department of Biomedical Engineering, Oregon Health & Science University, Portland, Oregon 97201, United States;* ● orcid.org/0000-0002-0597-0255; Email: nan@ohsu.edu

Authors

Stephen Palani − *Knight Cancer Early Detection Advanced Research Center, Oregon Health & Science University, Portland, Oregon 97201, United States; Department of Biomedical Engineering, Oregon Health & Science University, Portland, Oregon 97201, United States;* Present Address: Applied Materials, Santa Clara, CA 95054, United States

John P. Kenison − *Knight Cancer Early Detection Advanced Research Center, Oregon Health & Science University, Portland, Oregon 97201, United States;* Present Address: Picarro Inc., Santa Clara, CA 95054, United States.; ● orcid.org/0000-0003-4138-6600

Sinan Sabuncu − *Knight Cancer Early Detection Advanced Research Center, Oregon Health & Science University, Portland, Oregon 97201, United States;* ● orcid.org/0000-0001-8346-8175

Tao Huang − *Department of Biomedical Engineering, Oregon Health & Science University, Portland, Oregon 97201, United States;* Present Address: KLA-Tencor, Hillsboro, OR 97006, United States.

Fehmi Civitci − *Knight Cancer Early Detection Advanced Research Center, Oregon Health & Science University, Portland, Oregon 97201, United States;* Present Address: Apple Inc., Cupertino, CA 95014, United States.

Sadik Esener − *Knight Cancer Early Detection Advanced Research Center, Oregon Health & Science University, Portland, Oregon 97201, United States; Department of Biomedical Engineering, Oregon Health & Science University, Portland, Oregon 97201, United States*

Complete contact information is available at:
https://pubs.acs.org/10.1021/acsnano.2c08702

Author Contributions

X.N. conceived the project. T.H., F.C., J.P.K., and X.N. designed and constructed the microscope configuration. S.P., T.H., and F.C. developed software for data acquisition and analysis. S.P. and X.N. designed and performed single-particle LSPR measurements. S.P. and S.S. performed TEM measurements. S.P., X.N., S.S., and S.E. wrote and revised the manuscript. X.N. and S.E. supervised the research. All authors have given approval to the final version of the manuscript.

REFERENCES

(1) Mody, V. V.; Siwale, R.; Singh, A.; Mody, H. R. Introduction to metallic nanoparticles. *J. Pharm. Bioallied Sci.* **2010**, *2* (4), 282−289.

(2) Yang, J.; Giessen, H.; Lalanne, P. Simple Analytical Expression for the Peak-Frequency Shifts of Plasmonic Resonances for Sensing. *Nano Lett.* **2015**, *15* (5), 3439−3444.

(3) Nusz, G. J.; Marinakos, S. M.; Curry, A. C.; Dahlin, A.; Höök, F.; Wax, A.; Chilkoti, A. Label-Free Plasmonic Detection of Biomolecular Binding by a Single Gold Nanorod. *Anal. Chem.* **2008**, *80* (4), 984−989.

(4) Sriram, M.; Zong, K.; Vivekchand, S. R.; Gooding, J. J. Single nanoparticle plasmonic sensors. *Sensors (Basel)* **2015**, *15* (10), 25774−25792.

(5) McFarland, A. D.; Van Duyne, R. P. Single Silver Nanoparticles as Real-Time Optical Sensors with Zeptomole Sensitivity. *Nano Lett.* **2003**, *3* (8), 1057−1062.

(6) Zijlstra, P.; Paulo, P. M. R.; Orrit, M. Optical detection of single non-absorbing molecules using the surface plasmon resonance of a gold nanorod. *Nat. Nanotechnol.* **2012**, *7* (6), 379−382.

(7) Ament, I.; Prasad, J.; Henkel, A.; Schmachtel, S.; Sönnichsen, C. Single Unlabeled Protein Detection on Individual Plasmonic Nanoparticles. *Nano Lett.* **2012**, *12* (2), 1092−1095.

(8) Beuwer, M. A.; Prins, M. W. J.; Zijlstra, P. Stochastic Protein Interactions Monitored by Hundreds of Single-Molecule Plasmonic Biosensors. *Nano Lett.* **2015**, *15* (5), 3507−3511.

(9) Kelly, K. L.; Coronado, E.; Zhao, L. L.; Schatz, G. C. The Optical Properties of Metal Nanoparticles: The Influence of Size, Shape, and Dielectric Environment. *J. Phys. Chem. B* **2003**, *107* (3), 668−677.

(10) Tao, A. R.; Habas, S.; Yang, P. Shape Control of Colloidal Metal Nanocrystals. *Small* **2008**, *4* (3), 310−325.

(11) Xia, Y.; Xiong, Y.; Lim, B.; Skrabalak, S. E. Shape-Controlled Synthesis of Metal Nanocrystals: Simple Chemistry Meets Complex Physics? *Angew. Chem., Int. Ed.* **2009**, *48* (1), 60−103.

(12) Xia, Y.; Gilroy, K. D.; Peng, H.-C.; Xia, X. Seed-Mediated Growth of Colloidal Metal Nanocrystals. *Angew. Chem., Int. Ed.* **2017**, *56* (1), 60−95.

(13) Saha, K.; Agasti, S. S.; Kim, C.; Li, X.; Rotello, V. M. Gold nanoparticles in chemical and biological sensing. *Chem. Rev.* **2012**, *112* (5), 2739−2779.

(14) Vigderman, L.; Khanal, B. P.; Zubarev, E. R. Functional Gold Nanorods: Synthesis, Self-Assembly, and Sensing Applications. *Adv. Mater.* **2012**, *24* (36), 4811−4841.

(15) Huang, X.; Neretina, S.; El-Sayed, M. A. Gold Nanorods: From Synthesis and Properties to Biological and Biomedical Applications. *Adv. Mater.* **2009**, *21* (48), 4880−4910.

(16) Becker, J.; Trügler, A.; Jakab, A.; Hohenester, U.; Sönnichsen, C. The Optimal Aspect Ratio of Gold Nanorods for Plasmonic Biosensing. *Plasmonics* **2010**, *5* (2), 161−167.

(17) Nusz, G. J.; Curry, A. C.; Marinakos, S. M.; Wax, A.; Chilkoti, A. Rational Selection of Gold Nanorod Geometry for Label-Free Plasmonic Biosensors. *ACS Nano* **2009**, *3* (4), 795−806.

(18) John, C. L.; Xu, S.; Jin, Y.; Strating, S. L.; Zhao, J. X. Synthesis and Applications of Gold Nanorods. In *Trace Analysis with*

Nanomaterials; Pierce, D. T., Zhao, J. X., Eds.; Wiley: 2010; pp 359−381.

(19) Chow, T. H.; Li, N.; Bai, X.; Zhuo, X.; Shao, L.; Wang, J. Gold Nanobipyramids: An Emerging and Versatile Type of Plasmonic Nanoparticles. *Acc. Chem. Res.* **2019**, *52* (8), 2136−2146.

(20) Shen, H.; Lu, G.; Zhang, T.; Liu, J.; Gu, Y.; Perriat, P.; Martini, M.; Tillement, O.; Gong, Q. Shape effect on a single-nanoparticle-based plasmonic nanosensor. *Nanotechnology* **2013**, *24* (28), 285502.

(21) Halas, N. J.; Lal, S.; Chang, W.-S.; Link, S.; Nordlander, P. Plasmons in Strongly Coupled Metallic Nanostructures. *Chem. Rev.* **2011**, *111* (6), 3913−3961.

(22) Zamora-Perez, P.; Pelaz, B.; Tsoutsi, D.; Soliman, M. G.; Parak, W. J.; Rivera-Gil, P. Hyperspectral-enhanced dark field analysis of individual and collective photo-responsive gold−copper sulfide nanoparticles. *Nanoscale* **2021**, *13* (31), 13256−13272.

(23) Xiao, C.; Izquierdo-Roca, V.; Rivera-Gil, P. Real time and spatiotemporal quantification of pH and H2O2 imbalances with a multiplex SERS nanosensor. *Research Square* **2022**, 1.

(24) Peters, S. M.; Verheijen, M. A.; Prins, M. W.; Zijlstra, P. Strong reduction of spectral heterogeneity in gold bipyramids for single-particle and single-molecule plasmon sensing. *Nanotechnology* **2016**, *27* (2), 024001.

(25) Huang, T.; Phelps, C.; Wang, J.; Lin, L. J.; Bittel, A.; Scott, Z.; Jacques, S.; Gibbs, S. L.; Gray, J. W.; Nan, X. Simultaneous Multicolor Single-Molecule Tracking with Single-Laser Excitation via Spectral Imaging. *Biophys. J.* **2018**, *114* (2), 301−310.

(26) Phelps, C.; Huang, T.; Wang, J.; Nan, X. Multipair Förster Resonance Energy Transfer via Spectrally Resolved Single-Molecule Detection. *J. Phys. Chem. B* **2022**, *126* (31), 5765−5771.

(27) Liu, G. L.; Doll, J. C.; Lee, L. P. High-speed multispectral imaging of nanoplasmonic array. *Opt. Express* **2005**, *13* (21), 8520−8525.

(28) Fairbairn, N.; Christofidou, A.; Kanaras, A. G.; Newman, T. A.; Muskens, O. L. Hyperspectral darkfield microscopy of single hollow gold nanoparticles for biomedical applications. *Phys. Chem. Chem. Phys.* **2013**, *15* (12), 4163−4168.

(29) Zamora-Perez, P.; Tsoutsi, D.; Xu, R.; Rivera-Gil, P. Hyperspectral-Enhanced Dark Field Microscopy for Single and Collective Nanoparticle Characterization in Biological Environments. *Materials* **2018**, *11* (2), 243.

(30) Lumdee, C.; Yun, B.; Kik, P. G. Wide-Band Spectral Control of Au Nanoparticle Plasmon Resonances on a Thermally and Chemically Robust Sensing Platform. *J. Phys. Chem. C* **2013**, *117* (37), 19127−19133.

(31) Fakhrullin, R.; Nigamatzyanova, L.; Fakhrullina, G. Dark-field/hyperspectral microscopy for detecting nanoscale particles in environmental nanotoxicology research. *Science of The Total Environment* **2021**, *772*, 145478.

(32) Wei, Z.; Qi, H.; Li, M.; Tang, B.; Zhang, Z.; Han, R.; Wang, J.; Zhao, Y. Watching Single Gold Nanorods Grow. *Small* **2012**, *8* (9), 1331−1335.

(33) Nikoobakht, B.; El-Sayed, M. A. Preparation and Growth Mechanism of Gold Nanorods (NRs) Using Seed-Mediated Growth Method. *Chem. Mater.* **2003**, *15* (10), 1957−1962.

(34) Carbó-Argibay, E.; Rodríguez-González, B.; Gómez-Graña, S.; Guerrero-Martínez, A.; Pastoriza-Santos, I.; Pérez-Juste, J.; Liz-Marzán, L. M. The Crystalline Structure of Gold Nanorods Revisited: Evidence for Higher-Index Lateral Facets. *Angew. Chem., Int. Ed.* **2010**, *49* (49), 9397−9400.

(35) Goris, B.; Bals, S.; Van den Broek, W.; Carbó-Argibay, E.; Gómez-Graña, S.; Liz-Marzán, L. M.; Van Tendeloo, G. Atomic-scale determination of surface facets in gold nanorods. *Nat. Mater.* **2012**, *11* (11), 930−935.

(36) Kaushal, S.; Nanda, S. S.; Yi, D. K.; Ju, H. Effects of Aspect Ratio Heterogeneity of an Assembly of Gold Nanorod on Localized Surface Plasmon Resonance. *J. Phys. Chem. Lett.* **2020**, *11* (15), 5972−5979.

(37) Hu, M.; Novo, C.; Funston, A.; Wang, H.; Staleva, H.; Zou, S.; Mulvaney, P.; Xia, Y.; Hartland, G. V. Dark-field microscopy studies of single metal nanoparticles: understanding the factors that influence the linewidth of the localized surface plasmon resonance. *J. Mater. Chem.* **2008**, *18* (17), 1949−1960.

(38) Hoggard, A.; Wang, L.-Y.; Ma, L.; Fang, Y.; You, G.; Olson, J.; Liu, Z.; Chang, W.-S.; Ajayan, P. M.; Link, S. Using the Plasmon Linewidth To Calculate the Time and Efficiency of Electron Transfer between Gold Nanorods and Graphene. *ACS Nano* **2013**, *7* (12), 11209−11217.

(39) Rundqvist, J.; Hoh, J. H.; Haviland, D. B. Substrate effects in poly(ethylene glycol) self-assembled monolayers on granular and flame-annealed gold. *J. Colloid Interface Sci.* **2006**, *301* (1), 337−341.

(40) Rundqvist, J.; Hoh, J. H.; Haviland, D. B. Poly(ethylene glycol) Self-Assembled Monolayer Island Growth. *Langmuir* **2005**, *21* (7), 2981−2987.

(41) Cerruti, M.; Fissolo, S.; Carraro, C.; Ricciardi, C.; Majumdar, A.; Maboudian, R. Poly(ethylene glycol) Monolayer Formation and Stability on Gold and Silicon Nitride Substrates. *Langmuir* **2008**, *24* (19), 10646−10653.

(42) Chen, H.; Kou, X.; Yang, Z.; Ni, W.; Wang, J. Shape- and Size-Dependent Refractive Index Sensitivity of Gold Nanoparticles. *Langmuir* **2008**, *24* (10), 5233−5237.

(43) Lu, G.; Hou, L.; Zhang, T.; Li, W.; Liu, J.; Perriat, P.; Gong, Q. Anisotropic Plasmonic Sensing of Individual or Coupled Gold Nanorods. *J. Phys. Chem. C* **2011**, *115* (46), 22877−22885.

(44) Edelstein, A. D.; Tsuchida, M. A.; Amodaj, N.; Pinkard, H.; Vale, R. D.; Stuurman, N. Advanced methods of microscope control using *μ*Manager software. *Journal of Biological Methods* **2014**, *1* (2), e10.

(45) Nickerson, A.; Huang, T.; Lin, L.-J.; Nan, X. Photoactivated Localization Microscopy with Bimolecular Fluorescence Complementation (BiFC-PALM) for Nanoscale Imaging of Protein-Protein Interactions in Cells. *PLoS One* **2014**, *9* (6), e100589.

(46) Nickerson, A.; Huang, T.; Lin, L. J.; Nan, X. Photoactivated localization microscopy with bimolecular fluorescence complementation (Bifc-palm). *J. Visualized Exp.* **2015**, *2015* (106), 1.

(47) Chandradoss, S. D.; Haagsma, A. C.; Lee, Y. K.; Hwang, J.-H.; Nam, J.-M.; Joo, C. Surface Passivation for Single-molecule Protein Studies. *JoVE* **2014**, *86*, e50549.